nature materials

SUPPLEMENTARY INFORMATION

https://doi.org/10.1038/s41563-019-0380-x

In the format provided by the authors and unedited.

Bulk Dzyaloshinskii–Moriya interaction in amorphous ferrimagnetic alloys

Duck-Ho Kim[1*], Mitsutaka Haruta[1], Hye-Won Ko[2], Gyungchoon Go[3], Hyeon-Jong Park[2], Tomoe Nishimura[1], Dae-Yun Kim[4,5], Takaya Okuno[1], Yuushou Hirata[1], Yasuhiro Futakawa[6], Hiroki Yoshikawa[6], Wooseung Ham[1], Sanghoon Kim[1,7], Hiroki Kurata[1], Arata Tsukamoto[6], Yoichi Shiota[1], Takahiro Moriyama[1], Sug-Bong Choe[4], Kyung-Jin Lee[2,3] and Teruo Ono[1,8*]

[1]Institute for Chemical Research, Kyoto University, Kyoto, Japan. [2]KU-KIST Graduate School of Converging Science and Technology, Korea University, Seoul, Republic of Korea. [3]Department of Materials Science & Engineering, Korea University, Seoul, Republic of Korea. [4]Department of Physics and Institute of Applied Physics, Seoul National University, Seoul, Republic of Korea. [5]Center for Spintronics, Korea Institute of Science and Technology, Seoul, Republic of Korea. [6]College of Science and Technology, Nihon University, Funabashi, Chiba, Japan. [7]Department of Physics, University of Ulsan, Ulsan, Republic of Korea. [8]Center for Spintronics Research Network (CSRN), Graduate School of Engineering Science, Osaka University, Osaka, Japan. *e-mail: uzes.physics@gmail.com; ono@scl.kyoto-u.ac.jp

– Supplementary Information –

Bulk Dzyaloshinskii–Moriya Interaction in Amorphous Ferrimagnetic Alloys

Duck-Ho Kim[1*], Mitsutaka Haruta[1], Hye-Won Ko[2], Gyungchoon Go[3], Hyeon-Jong Park[2], Tomoe Nishimura[1], Dae-Yun Kim[4,5], Takaya Okuno[1], Yuushou Hirata[1], Yasuhiro Futakawa[6], Hiroki Yoshikawa[6], Wooseung Ham[1], Sanghoon Kim[1,7], Hiroki Kurata[1], Arata Tsukamoto[6], Yoichi Shiota[1], Takahiro Moriyama[1], Sug-Bong Choe[4], Kyung-Jin Lee[2,3], and Teruo Ono[1,8*]

[1]Institute for Chemical Research, Kyoto University, Uji, Kyoto 611-0011, Japan

[2]KU-KIST Graduate School of Converging Science and Technology, Korea University, Seoul 02841, Republic of Korea

[3]Department of Materials Science & Engineering, Korea University, Seoul 02841, Republic of Korea

[4]Department of Physics and Institute of Applied Physics, Seoul National University, Seoul 08826, Republic of Korea

[5]Center for Spintronics, Korea Institute of Science and Technology, Seoul, 02792, Republic of Korea

[6]College of Science and Technology, Nihon University, Funabashi, Chiba 274-8501, Japan

[7]Department of Physics, University of Ulsan, Ulsan 44610, Republic of Korea

[8]Center for Spintronics Research Network (CSRN), Graduate School of Engineering Science, Osaka University, Osaka 560-8531, Japan

[*]Correspondence to: uzes.physics@gmail.com (D.-H. Kim), ono@scl.kyoto-u.ac.jp (T. Ono)

Supplementary Text

Note S1. Tight-binding model of amorphous ferrimagnetic alloy.

To calculate Dzyaloshinskii-Moriya interaction (DMI) in amorphous ferrimagnetic alloys, we extend the zigzag chain model proposed by Kashid *et al.*[S1] (see Fig. S1). For simplicity, we consider a bilayer with varying the compositions of transition-metal (TM) and rare-earth (RE) atoms. The magnetic moments of TM and RE atoms are in the *x*-*z* plane and antiferromagnetically coupled.

In our calculation, we treat the spin-orbit interaction (SOI) as a perturbation. The total Hamiltonian $\mathcal{H}$ is[S1],

$$\mathcal{H} = \mathcal{H}_0 + \mathcal{H}_{\mathrm{mag}} + \mathcal{H}_{\mathrm{SO}}, \tag{S1}$$

where $\mathcal{H}_0$ is the spin-independent hopping elements and on-site energies, $\mathcal{H}_{\mathrm{mag}}$ is the s-d exchange interaction, and $\mathcal{H}_{\mathrm{SO}}$ is the SOI. Within first-order perturbation theory[S2], the energy correction from DMI is determined as

$$\delta\epsilon_n = \langle \mathrm{n}|\mathcal{H}_{\mathrm{SO}}|\mathrm{n}\rangle,$$

$$E_{\mathrm{DMI}} = \sum_{\mathrm{n}} \delta\epsilon_n \cdot f(\epsilon_n), \tag{S2}$$

where $|\mathrm{n}\rangle$ is the eigenvector of the Hamiltonian without the SOI, $\mathcal{H}_0 + \mathcal{H}_{mag}$, and $f(\epsilon_n)$ is the Fermi-Dirac distribution function. Based on these formulas, we perform tight-binding calculations considering *d*-orbitals in TM-RE zigzag chain (see Fig. S1).

For the perfectly ordered bilayer (i.e., maximally inversion asymmetric system), the

total Hamiltonian is written as,

$$\mathcal{H} = t_{\text{inter}} \sum_i \left(c_i^\dagger d_{i+1} + c_i^\dagger d_{i-1} + d_i^\dagger c_{i+1} + d_i^\dagger c_{i-1} \right) + t_{\text{TM}} \sum_i \left(c_i^\dagger c_{i+2} + c_i^\dagger c_{i-2} \right)$$
$$+ t_{\text{RE}} \sum_i \left(d_i^\dagger d_{i+2} + d_i^\dagger d_{i-2} \right) + E_{\text{TM}} \sum_i c_i^\dagger c_i + E_{\text{RE}} \sum_i d_i^\dagger d_i$$
$$+ J_{\text{TM}} \sum_i c_i^\dagger (\vec{\sigma} \cdot \vec{m}_{\text{TM}}) c_i + J_{\text{RE}} \sum_i d_i^\dagger (\vec{\sigma} \cdot \vec{m}_{\text{RE}}) d_i + \xi \left(\vec{L} \cdot \vec{\sigma} \right), \qquad \text{(S3)}$$

where $c_i^{(\dagger)}$ and $d_i^{(\dagger)}$ are annihilation (creation) operators of i^{th} TM and RE atoms, respectively (atomic numbers are given in zigzag order), $t_{\text{inter}}, t_{\text{TM}}, \text{and } t_{\text{RE}}$ are hopping parameters between TM-RE, TM-TM, and RE-RE, respectively, which are determined by the Slater-Koster integrals[S3], and $E_{\text{TM}} \text{ and } E_{\text{RE}}$ are on-site energies of TM and RE atoms, respectively. The s-d exchange energy of TM (RE) atom is given as $J_{\text{TM(RE)}}$, $\vec{\sigma}$ indicates the Pauli matrix, $\vec{L}$ is the orbital angular momentum, ξ is the atomic spin-orbit coupling, and $\vec{m}_{\text{TM(RE)}}$ is the (unit) magnetic moment of TM (RE) ion (see Table S1 for used parameters).

In this model, φ is the relative angle between magnetic moments of neighboring atoms and α is the bonding angle between different sites (see Fig. S1). The number of TM (RE) atom is chosen as 100 (100). Based on Eq. (S3) we compute the DMI energy for various cases of the composition gradient parameterized by $\mathcal{C}$ ($\equiv 1 - \frac{\text{n}_{\text{TM,upper}} - \text{n}_{\text{TM,lower}}}{\text{n}_{\text{TM,upper}} + \text{n}_{\text{TM,lower}}}$), where $\text{n}_{\text{A,B}}$ is the number of A atom in the B layer. To resemble amorphous RE-TM alloys, we randomly distribute RE and TM atoms in bilayers for a given $\mathcal{C}$. An increment of parameter $\mathcal{C}$ refers to the reduction of composition gradient across the bilayer. That is, $\mathcal{C} = 0$ corresponds to the perfectly ordered bilayer with maximum inversion asymmetry whereas $\mathcal{C} = 1$ corresponds to the perfectly random bilayer with vanishing overall composition gradient. For a specific $\mathcal{C}$, we estimate the DMI energy for 15 trials of randomized

configurations of atomic sites. Figures 4**b-e** of the main text show the DMI energies of every trials at certain $\mathcal{C}$ and Fig. 4**f** shows the averaged DMI values of these trials for various E_{F}.

Note S2. Characterization of the Films: the magnetic properties.

Magnetic properties of the GdFeCo films were measured by using superconducting quantum interference device (SQUID). Figure S2**a** shows the saturation magnetization M_{S} as a function of thickness of the GdFeCo layer t for GdFeCo, GdFeCo/Pt, and GdFeCo/Cu films, respectively. It clearly shows that M_{S} decreases with increasing t. Figure S2**b** shows the effective magnetic anisotropy energy K_{eff} as a function of t, for GdFeCo, GdFeCo/Pt, and GdFeCo/Cu films, respectively. The values for all samples are summarized in Supplementary Table S2.

Note S3. High magnification transmission electron microscopy (TEM) images of GdFeCo films.

Here, we characterized the structures of the specimens, using a STEM and EELS. Figures S3**a-c** show high magnification transmission electron microscopy (TEM) images of (**a**) 10 nm, (**b**) 30 nm, and (**c**) 50 nm GdFeCo films. It is shown that the GdFeCo layer in all the films has typical amorphous contrast across the wide range of the thickness in the film.

Note S4. Annealing temperature dependence of the DMI and analysis of laterally averaged line profiles of Gd/Fe.

To investigate annealing temperature effect on DMI, we first prepared 30-nm GdFeCo/Pt films. Then the films were annealed in a vacuum anneal oven in a field of 0.2 T along the in-plane direction. Each of films was annealed at a series of increasing anneal temperatures for 1 hour at each temperature indicated. Successive anneal temperatures were increased by typically 50 °C. Figures S4**a-d** show the measured $(\mu_0 H_c)^{1/2}$ as a function of $\mu_0 H_x$ for each annealing temperature T_a =0, 50, 100, 150, and 200 °C, respectively. These figures clearly show that $(\mu_0 H_c)^{1/2}$ as a function of $\mu_0 H_x$ exhibits a threshold point, which corresponds to $\mu_0 H_{DMI}$ (indicated by purple arrows). The red solid lines in Figs. S4**a-c** show the best fits based on the magnetic droplet nucleation model. The good conformity supports the validity of this model. Figure S5 shows T_a dependence of (**a**) $\mu_0 H_{DMI}$ and (**b**) D. It clearly shows that D increases monotonically with increasing T_a, but D is maximized at T_a =150 °C and then D decreases after an anneal at 150 °C, as shown in Fig. S5. Note that they were single domain phase with perpendicular magnetic anisotropy below 200 °C, however, magnetic properties were changed above an anneal at 200 °C, such as stripe domain phase with perpendicular magnetic anisotropy at T_a = 250 °C and in-plane magnetic anisotropy at T_a =300 °C.

Then, we investigated the elemental maps of each component of Gd, Fe, and Co for each T_a, respectively, as shown Figs. S6**a-h**. Then, we analyse laterally averaged line profiles of Figs. S6**a-h**. Figures 6**i-m** show laterally averaged line profiles of Gd/Fe with respect to z axis position for each T_a, where the orange boxes indicate the GdFeCo layer for each film. Figure S7**a** summarize β as a function of T_a. It shows that non-uniform profile along the direction of the GdFeCo thickness, which is represented by β, also has maximum at T_a = 150 °C. The correlation between β and D is also found in Fig. S7**b**, which is

consistent with the result as shown the inset of Fig. 3**t**.

Note S5. Estimation of the domain wall (DW) hard-axis anisotropy field.

The interfacial DMI energy density D can be defined as $D \equiv \lambda M_s \mu_0 H_{\mathrm{DMI}}$, thus it is natural small D in ferrimagnet compared with D in ferromagnet because M_s in ferrimagnet is 1 order smaller than M_s in ferromagnet. For stabilizing homochiral Néel DWs, we compare the Dzyaloshinskii-Moriya interaction induced effective magnetic field $\mu_0 H_{\mathrm{DMI}}$ and the domain-wall (DW) hard-axis anisotropy field $\mu_0 H_S$. If $\mu_0 H_{\mathrm{DMI}}$ is larger than $\mu_0 H_S$, a homochiral Neel DW can be stabilized initially. $\mu_0 H_S$ is estimated using the relation $\mu_0 H_S \cong \left(\frac{2\ln 2}{\pi^2}\right) \mu_0 M_S \lambda / t_f$ [S4,S5], where M_S is the saturation magnetization, t_f is the thickness of the magnetic layer, and λ is the DW width. The estimated $\mu_0 H_S$ is 0.9 mT by using $M_S = 10^4$ A/m, $\lambda = 15$ nm[S6], and $t_f = 30$ nm. Since $\mu_0 H_S$ is much smaller than $\mu_0 H_{DMI}$, homochiral Neel DW can be stabilized in our films. Although there is small D in ferrimagnet due to antiferromagnetic coupling between RE and TM elements inducing the small M_s, the stabilizing skyrmions can be generated in ferrimagnet in recent reports[S7] and thus the important factor for stabilizing homochiral Neel DW is the relative comparation between $\mu_0 H_S$ and $\mu_0 H_{\mathrm{DMI}}$.

Note S6. Estimation of the DW types from the asymmetric domain expansion.

To check the DW types (Neel or Bloch), we investigated the asymmetry in domain expansion patterns in these samples, following by the method described in Ref. S8. The

asymmetry in domain expansion patterns is caused by the counterbalance between the Dzyaloshinskii–Moriya and Zeeman interactions, which results in the elongation of the domains either longitudinal (for Neel-type DWs) or transverse (for Bloch-type DWs) to the in-plane magnetic field. Figure S8 shows the asymmetric domain expansion in 5 nm SiN/10 nm GdFeCo/100 nm SiN films. The elongation of the domain patterns is longitudinal to $\mu_0 H_x$ for (a) up domain and (b) down domain. Because the elongation is related with the chirality of the DWs[S8], the expansion patterns of the bubble domains with reversed magnetization. Other films also show the similar asymmetry in the same direction, which means the same sign of the DMI in all films. From the examining the elongation axis, we can conclude that all our films have the left-handed Neel-types DWs.

Note S7. Possible origin of the thickness-dependent change in the elemental composition of the GdFeCo film.

To find a possible origin of the thickness-dependent change in the elemental composition of the GdFeCo film, we characterized the spatial distribution (laterally averaged line profiles) of the elemental content in the cases of 5 nm SiN/30 nm GdFeCo/100 nm SiN film (Fig. S9**a**) and of 5 nm SiN/50 nm GdFeCo/100 nm SiN film (Fig. S9**b**) by high-angle a nnular dark field (HAADF) STEM images. It clearly shows that Si and N penetrate the GdFeCo layer and the penetration intensity is very different for GdFeCo films with different thickness (The orange boxes indicate the penetration of Si and N). It suggests that the influence of top SiN (capping layer) might be attributable to the interdiffusion at the upper GdFeCo/SiN interface[S9-S12]. One of the possible scenarios is the difference of the enthalpy of formation between GdN and FeN[S13].

As the enthalpy of formation of GdN is negatively larger than that of FeN, Gd has a stronger tendency form an alloy with N than Fe does. As a result, top layer Gd's concentration is much lower than Fe's concentration, resulting in the lower Gd/Fe concentration on the top (near capping layer). Because the DMI is independent of the buffer layer (SiN, Pt, or Cu), we believe that the difference of the enthalpy of formation between GdN and FeN could generate a gradual transition from one alloy, resulting the variation of the elemental composition of the GdFeCo film through the thickness, but it is needed to investigate further study to demonstrate the origin of this gradient through the thickness.

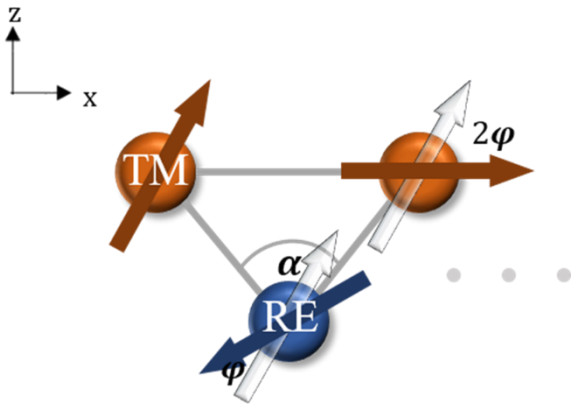

Figure S1. Schematic illustration of the zigzag chain model composed of TM and RE atoms.

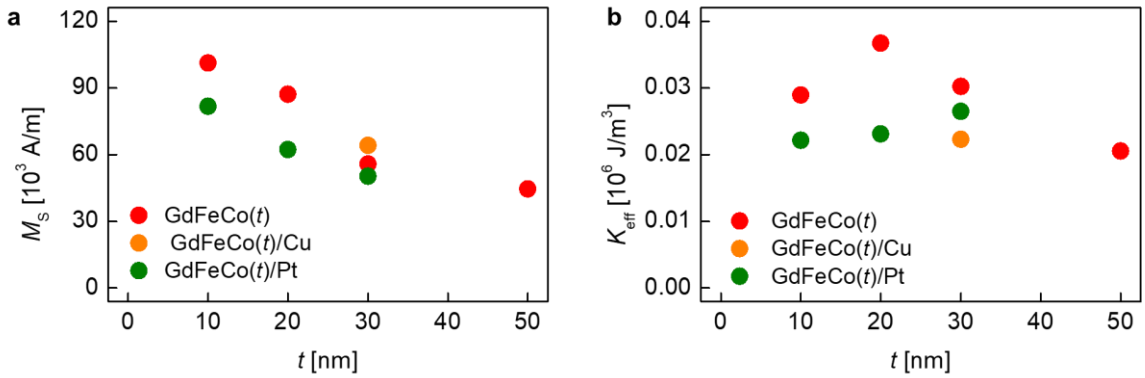

Figure S2. the magnetic properties for GdFeCo, GdFeCo/Pt, and GdFeCo/Cu films: a, The saturation magnetization M_S as a function of thickness of GdFeCo layer t. **b**, the effective magnetic anisotropy energy K_{eff} as a function of t.

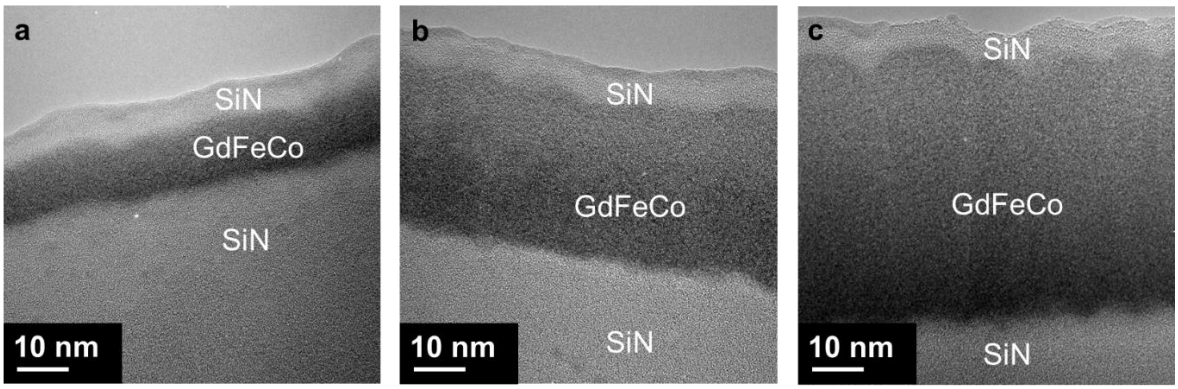

Figure S3. Characteristics of GdFeCo Films through STEM-EELS. a-c, High-magnification TEM images of (**a**) 10 nm, (**b**) 30 nm, and (**c**) 50 nm GdFeCo films.

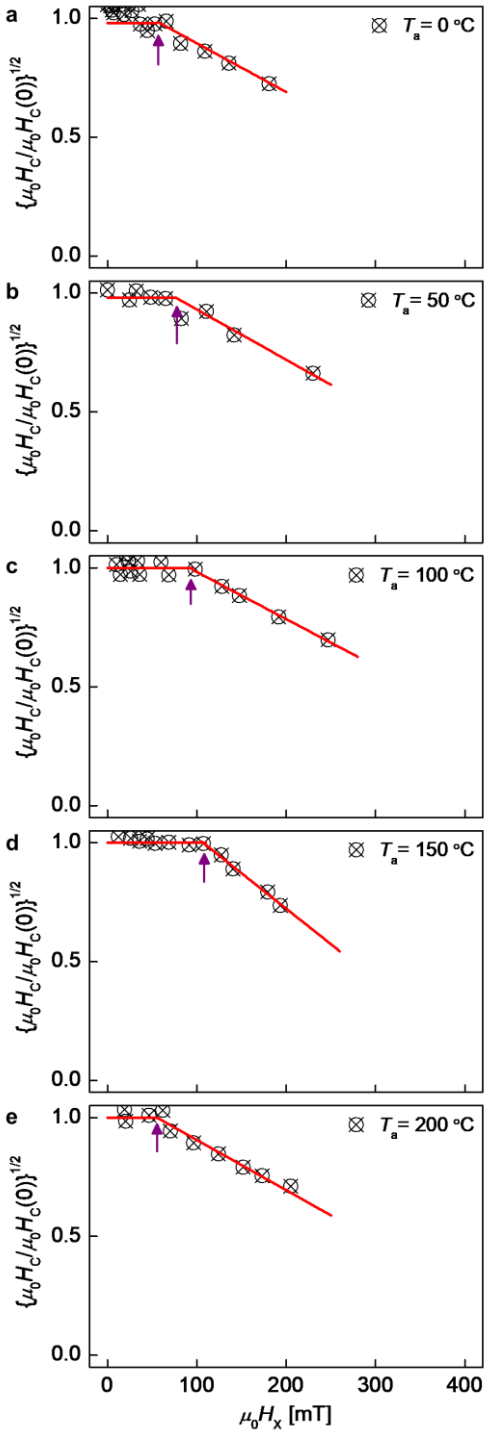

Figure S4. Measured $(\mu_0 H_c)^{1/2}$ as a function of $\mu_0 H_x$ for each annealing temperature T_a = (a) 0, (b) 50, (c) 100, (d) 150, and (e) 200 °C.

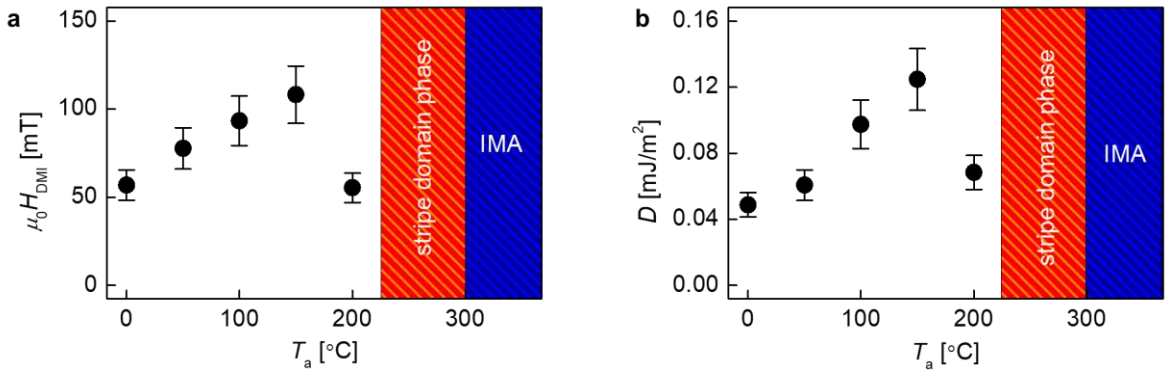

Figure S5. T_a **dependence of (a)** $\mu_0 H_{\mathrm{DMI}}$ **and (b)** D**.**

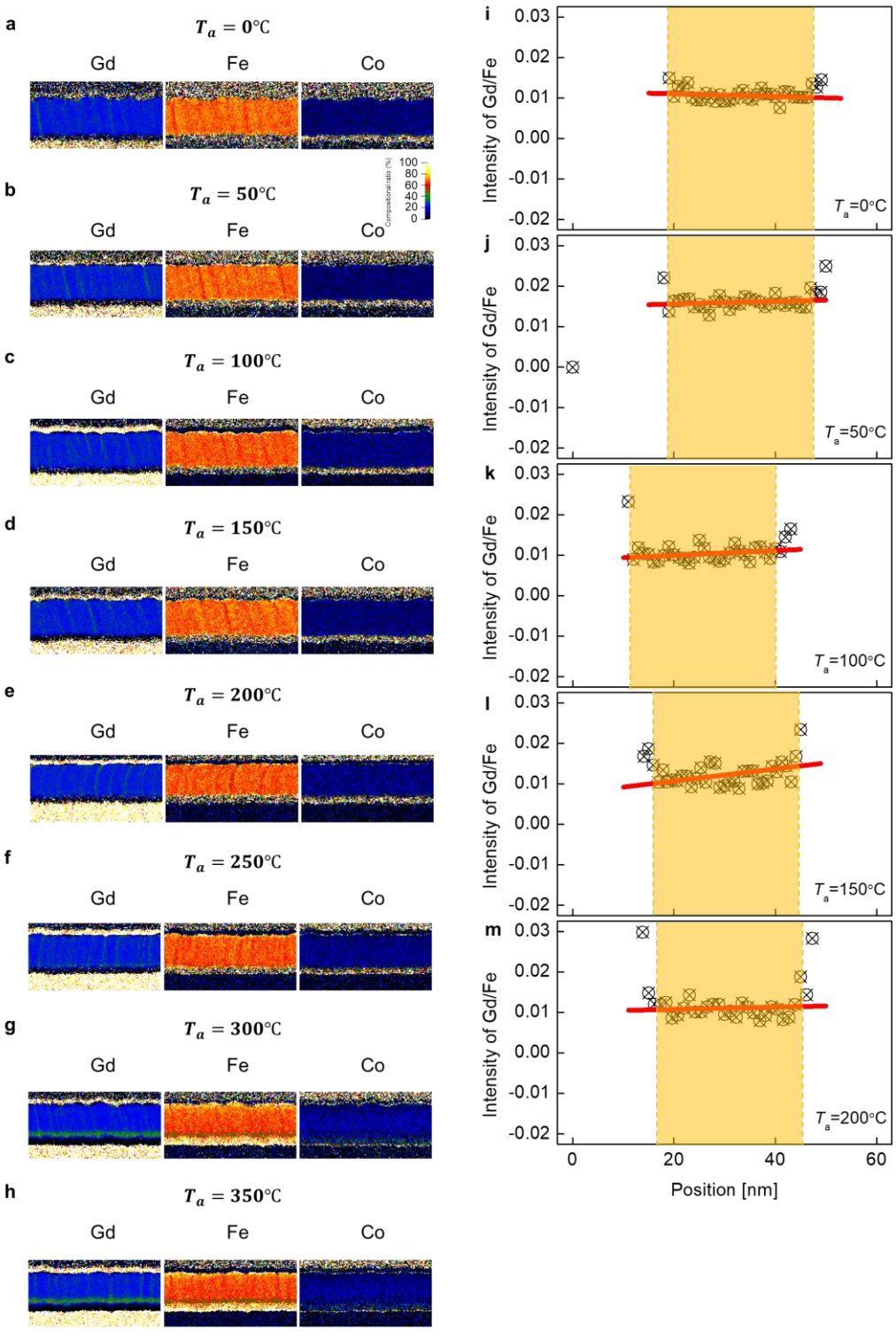

Figure S6. Elemental maps of each component of Gd, Fe, and Co for each T_a and laterally averaged line profiles of Gd/Fe with respect to z axis position for each T_a.

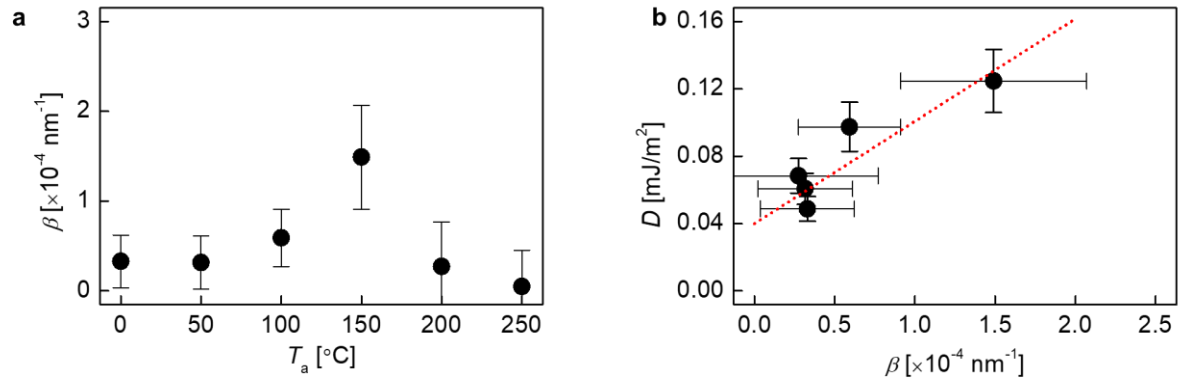

Figure S7. (a) β as a function of T_a. (b) D as a function of β.

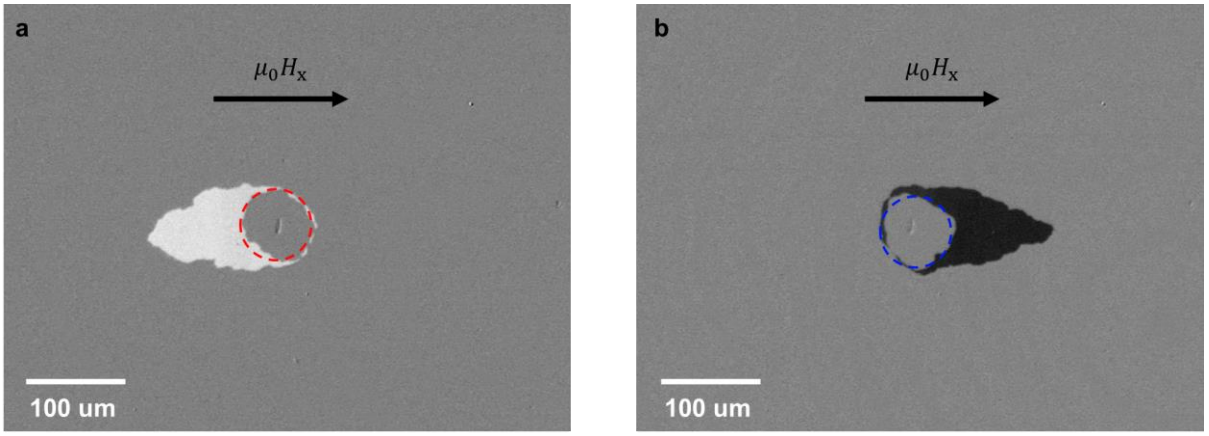

Figure S8. Image of the expansion patterns of (a) upward-pointing domain and (b) upward-pointing domain for 10 nm GdFeCo film. The dashed circle (red) indicates the initial up domain and the dashed circle (blue) the down domain.

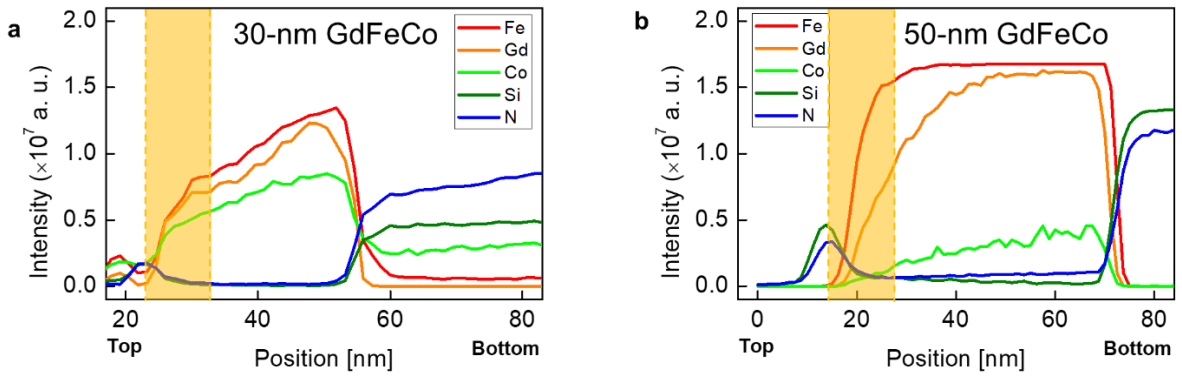

Figure S9. laterally averaged line profiles of Fe, Gd, Co, Si, and N for (a) 30 and (b) 50-nm thickness with respect to z axis position.

Supplementary Table S1. Tight-binding parameters.

Parameter		value
TM-TM	$V_{dd\sigma}$	-1.15 eV
	$V_{dd\pi}$	0.78 eV
	$V_{dd\delta}$	-0.05 eV
RE-RE	$V_{dd\sigma}$	-0.98 eV
	$V_{dd\pi}$	0.91 eV
	$V_{dd\delta}$	-0.07 eV
RE-TM	$V_{dd\sigma}$	-1.01 eV
	$V_{dd\pi}$	0.83 eV
	$V_{dd\delta}$	-0.12 eV
$\boldsymbol{E_{TM}}$		0.0 eV
$\boldsymbol{E_{RE}}$		1.0 eV
$\boldsymbol{J_{TM}}$		2.0 eV
$\boldsymbol{J_{RE}}$		1.2 eV
$\boldsymbol{\xi_{TM}}$		0.25 eV
$\boldsymbol{\xi_{RE}}$		0.60 eV
$\boldsymbol{\alpha}$		60°
$\boldsymbol{\varphi}$		30°

Supplementary Table S2. The saturation magnetization M_S and the effective magnetic anisotropy energy K_{eff}.

Name	Sample Structures	M_S [$\times 10^3$ A/m]	K_{eff} [J/m^3]
Sample I	10 nm $Gd_{25.0}Fe_{65.6}Co_{9.4}$/100 nm SiN	101.25	28946.98
Sample II	20 nm $Gd_{23.5}Fe_{66.9}Co_{9.6}$/100 nm SiN	87.14	36723.88
Sample III	30 nm $Gd_{23.5}Fe_{66.9}Co_{9.6}$/100 nm SiN	55.86	30238.13
Sample IV	50 nm $Gd_{23.5}Fe_{66.9}Co_{9.6}$/100 nm SiN	44.57	20564.51
Sample V	10 nm $Gd_{25.0}Fe_{65.6}Co_{9.4}$/5 nm Pt/100 nm SiN	81.73	22148.17
Sample VI	20 nm $Gd_{23.5}Fe_{66.9}Co_{9.6}$/5 nm Pt/100 nm SiN	62.26	23123.62
Sample VII	30 nm $Gd_{23.5}Fe_{66.9}Co_{9.6}$/5 nm Pt/100 nm SiN	50.27	26476.41
Sample VIII	30 nm $Gd_{23}Fe_{67.4}Co_{9.6}$/5 nm Cu/5 nm SiN	64.21	22327.92

References

S1. Kashid, V., Schena, T., Zimmermann, B., Mokrousov, Y., Blügel, S., Shah, V. & Salunke, H. G., Dzyaloshinskii-Moriya interaction and chiral magnetism in 3d-5d zigzag chains: Tight-binding model and ab initio calculations. Phys. Rev. B **90**, 054412 (2014).

S2. Heide, M., Bihlmayer, & G., Blügel, S., Describing Dzyaloshinskii-Moriya spirals from first principles. Phys. B: Condens. Matter **404**, 2678 (2009).

S3. Slater, J. C. & Koster, G. F., Simplified LCAO Method for the Periodic Potential Problem. Phys. Rev. **94**, 6 (1954).

S4. Jung, S.-W., Kim, W., Lee, T.-D., Lee, K.-J. & Lee, H.-W. Current-induced domain wall motion in a nanowire with perpendicular magnetic anisotropy. Appl. Phys. Lett. **92**, 202508 (2008).

S5. Kim, D.-Y., Kim, D.-H. & Choe, S.-B. Intrinsic asymmetry in chiral domain walls due to the Dzyaloshinskii–Moriya interaction. Appl. Phys. Express **9**, 053001 (2016).

S6. Kim, D.-H., Okuno, T., Kim, S. K., Oh, S.-H., Nishimura, T., Hirata, Y., Futakawa, Y., Yoshikawa, H., Tsukamoto, A., Tserkovnyak, Y., Shiota, Y., Moriyama, T., Kim, K.-J., Lee, K.-J. & Ono, T. Low magnetic damping of ferrimagnetic GdFeCo alloys. Phys. Rev. Lett. **122**, 127203 (2019).

S7. Woo, S., Song, K. M., Zhang, X., Zhou, Y., Ezawa, M., Liu, X., Finizio, S., Raabe, J., Lee, N. J., Kim, S.-I., Park, S.-Y., Kim, Y., Kim, J.-Y., Lee, D., Lee, O. J., Choi, J. W., Min, B.-C., Koo, H. C. & Chang, J. Current-driven dynamics and inhibition of the skyrmion Hall effect of ferrimagnetic skyrmions in GdFeCo films. Nat. Commun. **9**, 959 (2018).

S8. Kim, D.-Y., Kim, D.-H., Moon, J. & Choe, S.-B. Determination of magnetic domain-wall types using Dzyaloshinskii–Moriya-interaction-induced domain patterns. Appl. Phys. Lett. **106**, 262403 (2015).

S9. Bertero, G.A. & Sinclair, R. Kerr rotations and anisotropy in (Pt/Co/Pt)/X multilayers. IEEE. Trans. Magn. **31**, 3337-3342 (1995).

S10. Bandiera, S., Sousa, R. C., Rodmacq, B. & Dieny, B. Asymmetric Interfacial Perpendicular Magnetic Anisotropy in Pt/Co/Pt Trilayers. IEEE Magn. Lett. **2**, 3000504 (2011).

S11. Bandiera, S., Sousa, R. C., Rodmacq, B. & Dieny, B. Enhancement of perpendicular magnetic anisotropy through reduction of Co-Pt interdiffusion in (Co/Pt) multilayers. Appl. Phys. Lett. **100**, 142410 (2012).

S12. Kim, D.-H., Yoo, S.-C., Kim, D.-Y., Moon, K.-W., Je, S.-G., Cho, C.-G., Min, B.-C. & Choe, S.-B. Maximizing domain-wall speed via magnetic anisotropy adjustment in Pt/Co/Pt films. Appl. Phys. Lett. **104**, 142410 (2014).

S13. Kim, J., Lee, D., Lee, K.-J., Ju, B.-K., Koo, H. C., Min, B.-C. & Lee, O. Spin-orbit torques associated with ferrimagnetic order in Pt/GdFeCo/MgO layers. Sci. Rep. **8**, 6017 (2018).